A Soft, Steerable Continuum Robot that Grows via Tip Extension

Joseph D. Greer, Tania K. Morimoto, Allison M. Okamura, and Elliot W. Hawkes

***Abstract*— Soft continuum robots exhibit access and manipulation capabilities in constrained and cluttered environments not achievable by traditional robots. However, environmental contact can drastically alter the motion of continuum robots, complicating their control in these applications. Here we describe the design, modeling, and control of a soft continuum robot with a novel extension degree-of-freedom that enables movement in a direction that is always tangent to the robot's backbone, independent of environmental contacts. Steering occurs by inflating multiple Series Pneumatic Artificial Muscles (sPAMs) arranged radially around the backbone and extending along the robot's whole length. This design simplifies navigation of the robot by decoupling steering and extension. To navigate to a destination, the robot is steered to point at the destination, and the extension degree-of-freedom is used to reach it. We present models and experimentally verify the sPAMs and growing robot kinematics. The kinematic model has a mean position accuracy of 5.5 cm for predicting the tip position of a 42 cm long robot. Control of the growing robot is demonstrated using an eye-in-hand visual servo control law that enables growth of the robot to designated locations.**

I. INTRODUCTION

Because of their slender, continuously deformable, and compliant structures, continuum robots are useful for applications that require manipulation in or navigation through space-constrained and unstructured environments. Application areas of continuum robots are diverse and include minimally invasive surgery [1], [2], [3], search and rescue [4], and inspection [5], [6]. However, their continuum nature introduces a new set of challenges for modeling and control compared to their rigid counterparts [7], [8]. In particular, environmental contacts and disturbances may drastically alter the kinematics and dynamics of the robot bodies [9]. In this paper, we introduce a new soft pneumatic continuum robot with a novel extension degree of freedom that permits movement of the robot's tip in a direction that is always tangent to the robot's backbone, independent of environmental contacts and disturbances (Fig. 1). Among other benefits, this design simplifies control of the robot because steering and extension are decoupled.

The soft robot extends by growing from its tip and controls its direction of growth by bending. Growth of the thin-walled low density polyethylene robot body is achieved by pneumatically driven eversion at its tip. This method of growth was described by Mishima et al. [11] in 2003, without steering. Rösch et al. and Sadeghi et al. [12], [13] also developed devices that moved using tip eversion, with tip eversion driven by a motor rather than air pressure. Those devices were developed to penetrate granular material [14], [15]. Using a variant of tip eversion, Tsukagoshi et al. [16] developed an extending robot that was steerable by manual control. More recently, Hawkes et al. applied the concept of tip eversion to a novel growing robot [10] made of thin-walled polyethylene tubing. This method demonstrated a robot that could grow in length by two orders of magnitude. It was steered using discrete heading changes along its backbone that were permanent; once a turn was made, it could not be undone. The soft robot we present in this paper uses the same method of growth, but a different method of turning – reversible bending of the soft growing robot body.

Bending is achieved using series pneumatic artificial muscles (sPAMs) [17] that are attached along the length of the robot's body (Fig. 2). The sPAMs cause reversible bending by exerting a tension force on the robot body and play a similar role to actuated tendons in traditional continuum

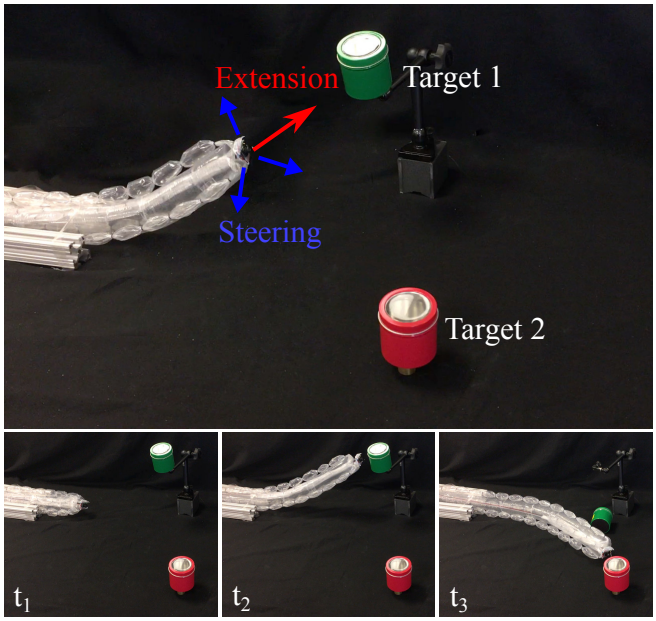

Fig. 1. Demonstration of soft continuum robot with novel extension degree of freedom. Extension is implemented with pneumatically driven tip eversion [10] and simplifies motion control of the robot's tip by decoupling steering and movement. The bottom row shows a sequence in which the robot autonomously navigates to Target 1, pushes the target off its perch, and then steers and lengthens to reach Target 2. Times in the sequence t_1, t_2, and t_3 are spaced approximately two seconds apart. A video of this demonstration is provided in the Supplementary Material.

This work was supported in part by National Science Foundation grant 1441358 and Air Force Office of Scientific Research grant FA2386-17-1-4658

[1]Department of Mechanical Engineering, Stanford University, Stanford, CA 94305 USA

[2]Department of Mechanical Engineering, University of California Santa Barbara, Santa Barbara, CA 93106 USA.

(e-mails: jdgreer@stanford.edu, taniakm@stanford.edu, aokamura@stanford.edu, and ewhawkes@engineering.ucsb.edu)

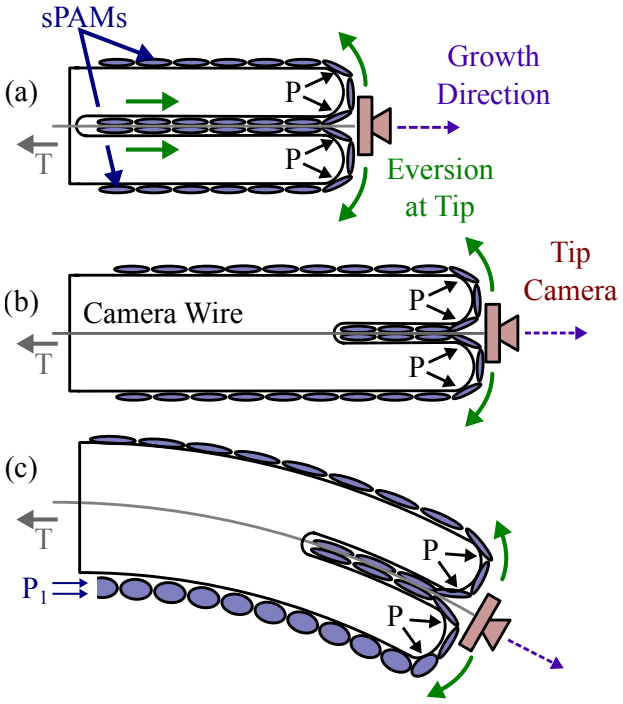

Fig. 2. Diagram of tip eversion based growth and steering, with a camera payload. (a) Growing robot in initial configuration. The body internal pressure, P, causes robot body and sPAMs, which are attached to the body along its length, to evert at the tip of the robot. Growth direction is indicated by the dashed arrow and is always approximately aligned with tip camera's optical axis. (b) After a period of time, the robot has lengthened as a result of the growth process. The tension force, T, on the camera wire keeps the camera positioned at the distal end of the robot. (c) Pressurizing the lower sPAM to a pressure, P_1, causes it to bulge and contract, resulting in constant curvature bending of the robot body downward.

robots [18]. A sPAM is a type of pneumatic artificial muscle (PAM) [19], which is a class of contractile actuators that turn the potential energy of compressed gas into mechanical work. Other examples of PAMs include McKibben Muscles [20], pouch motors [21], pleated PAMs [22], inverse PAMs [23], and antagonistic PAMs [24]. As required by the extension degree of freedom, sPAMs are entirely soft. This allows them to withstand the large deformations that are experienced by the robot body and actuators as they unfurl from the tip during the eversion process (Fig. 2).

To steer the robot, we present an eye-in-hand visual servo based heading controller [25]. A camera at the robot's tip (Fig. 2) whose optical axis is aligned with the axis of the robot's backbone provides a point-of-view image from the robot's perspective. Using this image, an operator may designate a destination (e.g. an object of interest). Growth of the robot will result in the robot moving toward the destination. The reversibility of the bending actuators provides three advantages over the irreversible turning system presented in [10]. First, the robot can reach multiple targets in one growth cycle. Second, mistakes in steering can be corrected. Third, the operator can reorient the robot/camera to look at different features in its environment without having to grow in order to reorient.

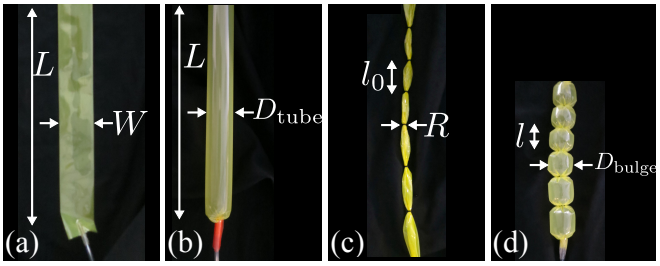

Fig. 3. Thin-walled polyethylene tubing (a) deflated and (b) inflated. An sPAM is a length of polyethylene tubing with o-rings spaced at regular intervals (c) deflated and (d) inflated.

The paper is organized as follows. Section II describes the design and fabrication of the growing robot. Section III develops a model for the kinematics of steering of the robot, which relates sPAM pressures and robot length, controlled by growth, to the location of the robot tip. Section IV introduces and analyzes a visual-servo based steering controller and demonstrates its effectiveness in tasks requiring the robot to steer to a goal location. A preliminary version of portions of this work appeared in conference form in [17], which introduced the sPAM actuator and steering of a *fixed length* robot. This study significantly extends [17] by adding growth as a degree of freedom to the robot, resulting in new models, control approaches, and robot capabilities.

II. Hardware

A. Robot

The growing robot is composed of a backbone and three sPAMs attached via double-sided tape radially around the backbone (Fig. 1). Both the backbone and the sPAMs start as flat sheets of thin-walled polyethlyene tubing of length L (Fig. 3(a). When inflated, the thin-walled polyethylene tubing takes on the shape of a cylinder (Fig. 3(b)). To create a sPAM, rubber o-rings are placed onto a tube at regular intervals along the length of the tube, creating a series of actuator segments among which air can flow. When the sPAM is inflated, the profile of each actuator segment between o-rings becomes bulged when compared to its deflated state (Fig. 3(c)). Assuming the material does not stretch significantly, the length of the actuator contracts when inflated due to its bulged profile (Fig. 3(d)).

As will be explained in Sec. III-B, the backbone can be thought of as a cantilevered beam whose stiffness is derived from its internal pressure. Similar to the motor-actuated tendons in certain continuum manipulators [18], the sPAMs exert moments on the pneumatic backbone to cause reversible bending of the robot. The three sPAMs provide controllability of the robot's yaw and pitch.

To place the robot in a state ready for growth, the assembled backbone and sPAMs are inverted and pushed into the center of the backbone until the backbone length is a fraction of its original length. When the main tube is pressurized, the robot everts from the tip and grows back to its original length as shown in Fig. 2. During the growth process, a camera is kept at the tip of the robot by applying a constant tension

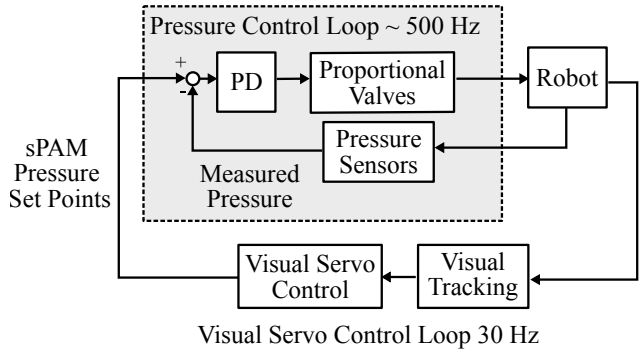

Fig. 4. Robot steering control architecture. An eye-in-hand visual servo controller running at the camera acquisition rate, 30 Hz, generates pressure set points for the three sPAMs. A lower-level pressure controller running at approximately 500 Hz maintains these desired pressures in the three sPAMs.

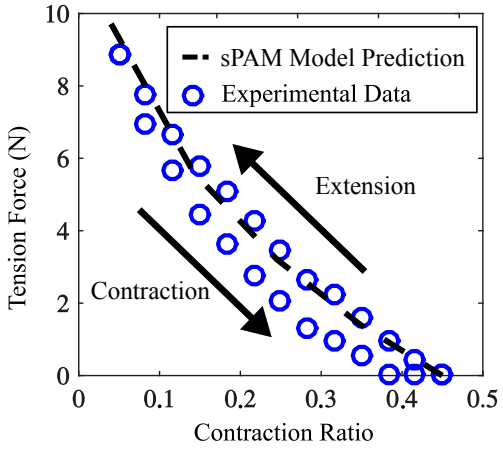

Fig. 5. Experimental force-displacement curve vs. predicted force-displacement curve of an sPAM.

force on the camera wire. This force can be supplied by hand or through other means such as a weight, friction clamp, or actuator. The backward tension on the camera also serves to throttle the rate of growth of the robot.

B. Pneumatic System

To control the growth rate and heading of the growing robot, pressure in the main tube and each of the three sPAMs is regulated. The main tube is controlled to a pressure appropriate for growth, between 6.9 and 20.7 kPa, with a pressure regulator valve. Pressure in each sPAM is dynamically adjusted during the course of growth of the robot to achieve a desired heading. Fig. 4 provides a high-level block diagram of the steering control architecture, in which the pneumatic system operates to regulate pressure. Pressure set-points for the pneumatic backbone and three sPAMs are regulated at 500 Hz by the pressure controller and commanded at 30 Hz by a visual servo controller (Sec. II-C). The pressure controller operates the pneumatic system, which consists of electronic proportional valves (EV-P-20-6050, Clippard Incorporated, Cincinnati, OH), that control air flow rates and analog pressure sensors (MPX5100DP-ND, Freescale Semiconductor, Austin, TX) that measure pressure in the three sPAMs.

C. Vision System

As explained in Sec. IV, an eye-in-hand visual servo control law [25] is used to orient the robot toward a user-defined goal position. Visual features are observed using a 170° field-of-view miniature camera (AccFly, Shenzhen, China) mounted at the tip of the continuum robot (Fig. 2). Image processing is performed by dedicated hardware (Sightline Applications Incorporated, Hood River, OR) at 30 Hz. Information from the image processing hardware is communicated to the control system via RS-232.

III. Physical Robot Modeling

In this section, we develop a relationship between the pressure inside each of the three sPAMs attached to the robot's body and the body's position in space. We start with a model of the sPAM relating internal pressure to tension force. We then use the sPAM model in a static force analysis in order to relate sPAM pressure to robot tip displacement. We conclude with an analysis of the workspace of the robot. For a more thorough treatment of the sPAM model, we refer the reader to [17].

A. sPAM Model

In previous work [17], it was established that when the o-ring spacing of an sPAM is below a threshold, the behavior of the actuators is identical to the behavior of pleated pneumatic artificial muscles (PPAMs). PPAMs were characterized by Daerden et al. [26] and have a known force-displacement relationship. The force-displacement curve of sPAMs was shown in [17] to have two important properties for the purposes of kinematic modeling:

1) The force-displacement curve is approximately linear (Fig. 5).
2) For a given displacement, force scales linearly with pressure, which may be seen from the length to load relationship of PAMs [22]:

$$F = -p\frac{\mathrm{d}V}{\mathrm{d}L} \tag{1}$$

where F is the force exerted by the actuator, p is the pressure inside the actuator, V is the volume inside the actuator and L is the length of the actuator along the direction F acts.

Given these two properties, we approximate each of the three sPAMs as linear springs with constant equilibrium lengths. Increasing or decreasing the pressure inside an sPAM changes the spring stiffness of the sPAM accordingly:

$$F_i = K_i(l_i - l_i^{\mathrm{eq}}) \qquad \text{for sPAM } i = 1,2,3 \tag{2}$$

where

$$K_i = p_i k_i \qquad \text{for sPAM } i = 1,2,3 \tag{3}$$

and F_i is the tension force, K_i is the spring stiffness, l_i is the length, l_i^{eq} is the equilibrium length, p_i is the pressure, and k_i is the scaling constant relating pressure to spring stiffness of the i^{th} sPAM.

B. Kinematics of Steering

Here we derive a kinematic model for steering of the growing robot. As explained in Sec. II, three sPAMs are attached radially around the robot's backbone and provide the ability to control the orientation of the tip of the robot in yaw and pitch. We make a simplifying assumption that tension force exerted by the sPAMs cause the robot to bend in a constant curvature arc [7] and that the sPAMs behave as linear springs. The model relates the three sPAM pressures, p_1, p_2, p_3, to position and orientation of the robot, $\vec{x}_{\text{ef}} \in \mathbb{R}^3$, $R_{\text{ef}} \in SO(3)$, respectively:

$$[\vec{x}_{\text{ef}}, R_{\text{ef}}]^\top = f(p_1, p_2, p_3) \tag{4}$$

Our kinematic model is developed in two steps: 1) First we use constant curvature continuum robot length kinematics to relate tendon lengths, l_1, l_2, l_3, to arc space parameters: backbone length, l, bending plane angle, ϕ, and pneumatic backbone radius of curvature, r (Fig. 6). 2) Second, we use static equilibrium force conditions of the soft continuum robot to develop relationships between the sPAM pressures and robot end effector position using the constant curvature constraints from part 1).

1) Constant curvature geometric kinematics: Here we review the work of Jones et al. [27] on the geometry of constant curvature continuum robots with direct control of tendon lengths, which computes arc-space parameters from side lengths. These will be used in step 2). We assume that the positions of the actuators on the robot's end piece, ψ_1, ψ_2, ψ_3, which are specified in angles, are known (Fig 6(d)). First we introduce three intermediate variables, which relate the positions of the actuators to the (unknown) position of the bending plane:

$$\phi_i = \psi_i - \phi \qquad \text{for sPAM } i = 1, 2, 3 \tag{5}$$

Using this definition, the robot tip geometry can be used to relate the (unknown) radii of curvatures of the three actuators to the (unknown) radius of curvature of the pneumatic backbone (Fig. 6(c))

$$r_i = r - (D_{\text{tube}}/2)\cos\phi_i \qquad \text{for sPAM } i = 1, 2, 3 \tag{6}$$

Multiplying Equation 6 by (unknown) θ and using the relation $l_i = \theta r_i$ we get

$$l_i = l - \theta(D_{\text{tube}}/2)\cos\phi_i \qquad \text{for sPAM } i = 1, 2, 3 \tag{7}$$

This yields three equations in our three unknown arc-space parameters, which can be solved assuming we know side lengths, l_1, l_2, l_3.

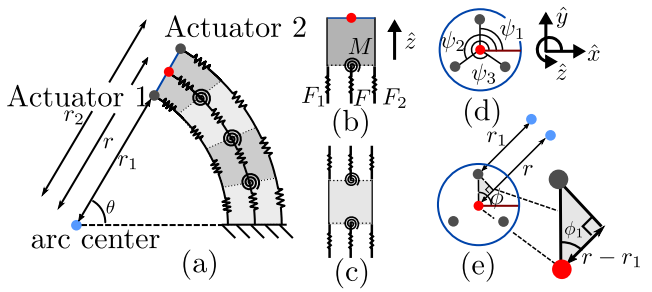

Fig. 6. (a) Kinematic model of constant curvature continuum robot. Cross-section in the bending plane of the continuum robot is shown. sPAMs are modeled as springs with stiffness controlled by actuator pressure. (b) End piece of spring system with forces acting on it. (c) Interior piece of spring system with forces acting on it. Sum of forces is always zero, independent of l and θ. (d) Head-on view of robot's tip. Actuators are arranged radially around tip center at angles ψ_1, ψ_2, ψ_3. (e) Head on view showing bending plane angle, ϕ and radii of curvatures of backbone and sPAM arc.

2) Static force analysis: Here we use static force balance to relate our input pressures, p_1, p_2, p_3, to arc space parameters, l, ϕ, r:

$$\sum \mathbf{F}(p_1, p_2, p_3, l, \phi, r) = 0 \tag{8}$$

$$\sum \mathbf{M}(p_1, p_2, p_3, l\phi, r) = 0 \tag{9}$$

In turn, the arc space parameters can be used to calculate $\vec{x}_{\text{ef}}$ and R_{ef}.

The pneumatic backbone has stiffness that resists both bending and compression. To model these characteristics, we discretize the robot along its length into N rigid arc elements, each of which subtends an angle θ/N as shown in Fig. 6(a). The pneumatic backbone's resistance to bending is captured as a series of torsion springs between each backbone segment with torsion spring constant, $\kappa^{(N)}$ and its resistance to axial compression is captured as a series of linear springs, each with stiffness $K^{(N)}$ and equilibrium length l_N^{eq}. We assume there is an underlying stiffness of the pneumatic backbone that is related to pressure and has an associated torsion and linear spring constant associated with it, κ and K, respectively. We relate the underlying stiffnesses to the discretized stiffnesses by the following scaling laws

$$K^{(N)} = NK \qquad \kappa^{(N)} = N\kappa \tag{10}$$

as is standard with discrete spring models [28].

Next, we consider the sPAMs. Because the force-displacement curves of our sPAMs are approximately linear (Fig. 5), we incorporate them into our model as linear springs. Each sPAM has a spring constant that scales linearly with pressure (Equation 3), $K_i = p_i k_i$, and an associated equilibrium length, l_i^{eq}. To incorporate our actuators into the distributed spring model, we break our actuators into N springs in series. Following the same convention as the main tube, we relate the N spring constants and equilibrium lengths to the actuator's spring constant by the following scaling law

$$K_i^{(N)} = NK_i \qquad \text{for } i = 1, 2, 3 \tag{11}$$

$$l_i^{(N)\text{eq}} = l_i^{\text{eq}}/N \qquad \text{for } i = 1, 2, 3 \tag{12}$$

With all elements of the system defined, we consider equilibrium conditions of the system. Internal pieces of the spring system (Fig. 6(c)) are in equilibrium regardless of the kinematic parameters, therefore they are not considered. For an end-piece of the spring system (Fig. 6(b)) to satisfy equilibrium, the sum of all forces must equal zero:

$$\left(\sum_{i=1}^{3} F_i + F\right)\hat{z} = \left(\sum_{i=1}^{3} -K_i(l_i - l_i^{\text{eq}}) - K(l - l^{\text{eq}})\right)\hat{z} = 0 \tag{13}$$

as well as the sum of moments about the pivot point of the discretized blocks:

$$\sum_{i=1}^{3} \mathbf{M}_i + \mathbf{M} = \\ = \sum_{i=1}^{3} \left(\frac{D_{\text{tube}}}{2} K_i(l_i - l_i^{\text{eq}}) R_{z'}(\psi_i)\right)\hat{y} - \kappa\theta R_{z'}(\phi)\hat{y} = 0 \tag{14}$$

where $R_{z'}(\,\cdot\,)$ is a rotation about the axis parallel to the tip of the robot by a specified angle.

The force and moment balance relations (Equations 13 and 14) reduce to three scalar equations in six unknowns ($\phi, \theta, l, l_1, l_2, l_3$). Including the geometric equations relating side lengths to l, ϕ, r (Equation 7) provides three more constraints, yielding a solvable system of six equations in six unknowns.

Finally, with l, ϕ, r computed, the end-effector position can be found. We define a coordinate system whose origin is at the base of the robot's backbone curve and coordinate axes that are parallel to those shown in Figure 6(d). With this coordinate system definition, we write $\vec{x}_{\text{ef}}$ and R_{ef} as

$$\vec{x}_{\text{ef}} = r(\cos(\theta) - 1)\hat{w} + r\sin(\theta)\hat{z} \tag{15}$$
$$\hat{w} = [\cos(\phi)\ \ \sin(\phi)\ \ 0]^\top \tag{16}$$
$$R_{\text{ef}} = R_v(\theta) \tag{17}$$
$$\hat{v} = [\sin(\phi)\ \ \cos(\phi)\ \ 0]^\top \tag{18}$$

C. Kinematics of Growth and Steering

Because backbone equilibrium length continuously increases during the growth process, we further analyze the effect backbone equilibrium length has on the kinematics of steering. As explained in Sec. III-B, Eqs. 7,13,14 provide six scalar equations in six unknowns that can be solved for: bending plane angle, radius of curvature, backbone length, and three side lengths ($\phi, r, l, l_1, l_2, l_3$). These equations are a function of known sPAM pressures, p_1, p_2, p_3, and robot geometry including backbone equilibrium length, l_{eq}. To analyze the effect of growth on steering kinematics, we assume that p_1, p_2, p_3 remain constant, and consider what happens if the backbone equilibrium length is changed from l_{eq} to αl_{eq}, for some constant $\alpha > 0$. The main result is that if the robot is grown with constant sPAM pressures, bending plane angle and curvature will remain constant.

To show this, we first return to the geometric relations of Eq. 7 and assume that l_i, θ, ϕ satisfy this equation for the original length, l:

$$l_i = l - \theta(D_{\text{tube}}/2)\cos\phi_i \qquad \text{for sPAM } i = 1, 2, 3 \tag{19}$$

Assuming this is true, then arc-space parameters $\alpha l_i, \alpha\theta, \phi$ will satisfy the equation for new backbone length, αl:

$$\alpha l_i = \alpha l - \alpha\theta(D_{\text{tube}}/2)\cos\phi_i \qquad \text{for sPAM } i = 1, 2, 3 \tag{20}$$

Now, we consider the static equilibrium conditions. Returning to the spring length scaling laws (Eqs. 10, 11), we note that the sPAM and main tube springs will have a stiffness factors of $1/\alpha$ compared to the original length, l

$$K^{(\alpha)} = K/\alpha \tag{21}$$
$$\kappa^{(\alpha)} = \kappa/\alpha \tag{22}$$
$$K_i^{(\alpha)} = K_i/\alpha \tag{23}$$
$$\tag{24}$$

where $K^{(\alpha)}, \kappa^{(\alpha)}, K_i^{(\alpha)}$ denote the underlying stiffnesses of the robot with length αl. Evaluating the static equilibrium equations (Eqs. 13, 14) with the new arc-space parameters and stiffnesses, we get:

$$\left(\sum_{i=1}^{3} -\frac{K_i}{\alpha}(\alpha l_i - \alpha l_i^{\text{eq}}) - \frac{K}{\alpha}(\alpha l - \alpha l^{\text{eq}})\right)\hat{z} = 0 \tag{25}$$

and

$$\left(-\sum_{i=1}^{3} \frac{D_{\text{tube}}}{2}\frac{K_i}{\alpha}(\alpha l_i - \alpha l_i^{\text{eq}})R_z(\psi_i) - \frac{\kappa}{\alpha}\alpha\theta R_z(\phi)\right)\hat{x} = 0 \tag{26}$$

The parameter α can be canceled from the above two equations. From this it follows that if arc-space parameters l_i, θ, ϕ satisfy the equilibrium conditions for a robot with equilibrium length l_{eq}, then $\alpha l_i, \alpha\theta, \phi$ will satisfy the equilibrium conditions for a robot with backbone equilibrium length αl_{eq}.

This establishes the expected relationship between arc-space parameters of two robots with the same actuator

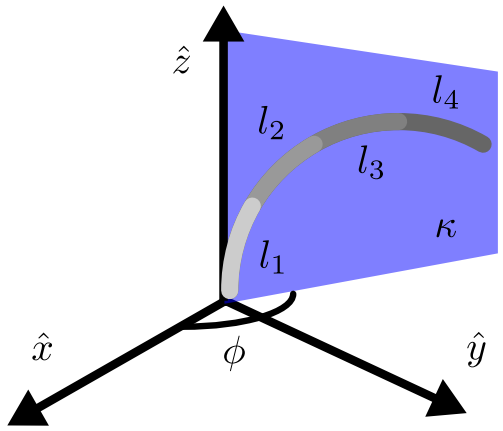

Fig. 7. Kinematics of the robot during growth. Eqs. 25 and 26 show that bending plane angle, ϕ, and backbone curvature, κ, will be constant during growth if sPAM pressures are constant.

pressures, p_1, p_2, p_3, but different equilibrium lengths, l_{eq}, and αl_{eq} (Fig. 7): the bending plane angle is conserved and the curvature of the robot will be the same ($\theta/l = \alpha\theta/\alpha l$).

D. Physical Jacobian

In this section, we explain how to compute the kinematic model's Jacobian, $J \in \mathbb{R}^{6\times 4}$, which maps from joint space velocities (i.e. growth rate, $\dot{\alpha}$, and pressure derivatives, $\dot{p_1}, \dot{p_2}, \dot{p_3}$) to the end-effector twist (linear and angular velocities):

$$[\dot{\vec{x}}_{\text{ef}}, \dot{\vec{\omega}}]^\top = J[\dot{\alpha}, \dot{p_1}, \dot{p_2}, \dot{p_3}]^\top \tag{27}$$

We decompose J as the product of two-matrices, $J_1 \in \mathbb{R}^{6\times 4}, J_2 \in \mathbb{R}^{6\times 6}$:

$$J = J_2 J_1 \tag{28}$$

J_1 maps joint-space velocities to arc-space parameter time-derivatives:

$$[\dot{\phi}, \dot{\theta}, \dot{l}, \dot{l_1}, \dot{l_2}, \dot{l_3}]^\top = J_1[\dot{\alpha}, \dot{p_1}, \dot{p_2}, \dot{p_3}]^\top \tag{29}$$

and J_2 maps arc-space parameter time-derivatives to end-effector twist:

$$[\dot{\vec{x}}_{\text{ef}}, \dot{\vec{\omega}}]^\top = J_2[\dot{\phi}, \dot{\theta}, \dot{l}, \dot{l_1}, \dot{l_2}, \dot{l_3}]^\top \tag{30}$$

Because we do not have a closed-form solution relating joint space parameters to arc-space parameters (Sec. III-C), we use the implicit function theorem to compute J_1:

$$J_1 = -\overbrace{\begin{bmatrix} \frac{\partial f_1}{\partial \phi} & \cdots & \frac{\partial f_1}{\partial l_3} \\ \vdots & \ddots & \vdots \\ \frac{\partial f_6}{\partial \phi} & \cdots & \frac{\partial f_6}{\partial l_3} \end{bmatrix}^{-1}}^{6\times 6} \overbrace{\begin{bmatrix} \frac{\partial f_1}{\partial \alpha} & \cdots & \frac{\partial f_1}{\partial p_3} \\ \vdots & \ddots & \vdots \\ \frac{\partial f_6}{\partial \alpha} & \cdots & \frac{\partial f_6}{\partial p_3} \end{bmatrix}}^{6\times 4} \tag{31}$$

where $f_1, \ldots, f_6$ are the kinematic constraint equations relating joint-space parameters to arc-space parameters (Eq. 20, 25, 26).

The equations relating arc-space parameters to position and orientation of the robot tip are explicit and therefore we compute J_2 by simply differentiating the expressions for $\vec{x}_{\text{ef}}$ and R_{ef} in equations 15 and 17 with respect to the arc-space parameters.

E. Workspace Analysis

Using the kinematic model developed in Sec. III-B and III-C, we can determine the set of points reachable by the tip of the growing robot, i.e. the growing robot's workspace. The inputs that are controllable include the equilibrium length of the backbone of the growing robot, αl_{eq}, and the sPAM pressures, p_1, p_2, p_3. To compute its workspace, we calculate the forward kinematics for each feasible input tuple:

$$(\alpha, p_1, p_2, p_3) \in [\alpha_{\min}, \alpha_{\max}] \times [0, p_{\max}]^3 \tag{32}$$

using Eqs. 6, 13, and 14. $\alpha_{\min}$ and $\alpha_{\max}$ represent the minimum and maximum backbone length ratios of the growing robot and $p_{\max}$ is the bursting pressure of the sPAMs.

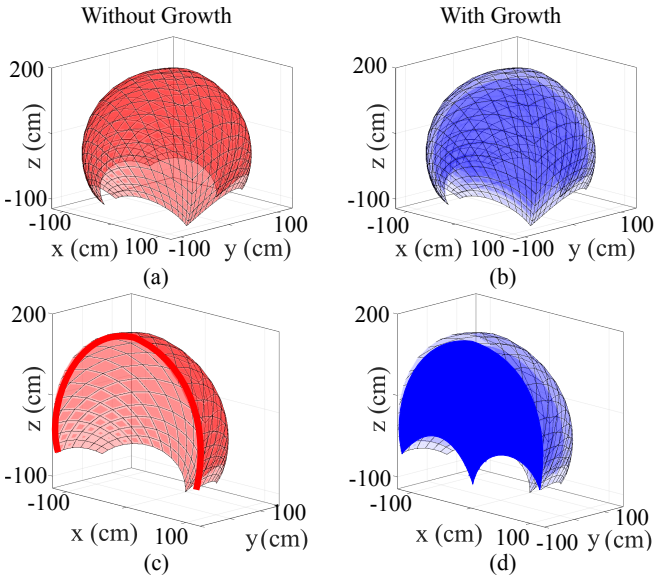

Fig. 8. Workspace analysis showing the positions achievable by the tip of a growing robot that is 200 cm long and whose base is at $(0, 0, 0)$. Without growth, (i.e. steering only) the robot tip is effectively confined to a two-dimensional steering surface (shown in (a) and a cross-section at $y = 0$ in (c)). With growth, the robot's workspace encompasses a solid three dimensional volume that is the union of steering surfaces of robots whose lengths range from 0 to 200 cm long (shown in (b) and a cross-section at $y = 0$ in (d)).

Figure 8 shows the workspace analysis for a robot that is 2 meters long when fully extended. At a fixed length of 2 meters, the robot tip can be steered along a set of points that is roughly a two-dimensional surface (Figs. 8(a) and (c)). We note that the steering surface is not exactly two-dimensional as the sPAMs may be used to reduce the length of the robot's backbone in addition to changing the orientation of the tip. Growth adds an independent degree of freedom that extends the workspace into a solid volume which is the union of steering surfaces of robots whose backbone equilibrium lengths vary from 0 to 2 meters (Figs. 8 (b) and (d)).

IV. Steering Control

In this section, we present and analyze the controller used to steer the robot. As explained in Sec. I, the robot's direction of growth is aligned with its tip tangent, and therefore the robot will grow to an object of interest if its heading is aligned with the object. To achieve heading alignment, we use a camera at the robot's tip, whose optical axis is parallel to the tip's tangent (Sec. II-C), and an an eye-in-hand visual servo controller (Fig. 9). The controller drives the object of interest's location within the camera's field of view to the center so that the robot's heading is aligned with the object.

A. Image space modeling

In this section, we derive the transformation from control inputs to image coordinates (Fig. 10), which is used in the visual servo control law. More concretely, using the notation of Chaumette [29], we let $\vec{s} \in \mathbb{R}^2$ be the image features we are interested in controlling (in this case, the image

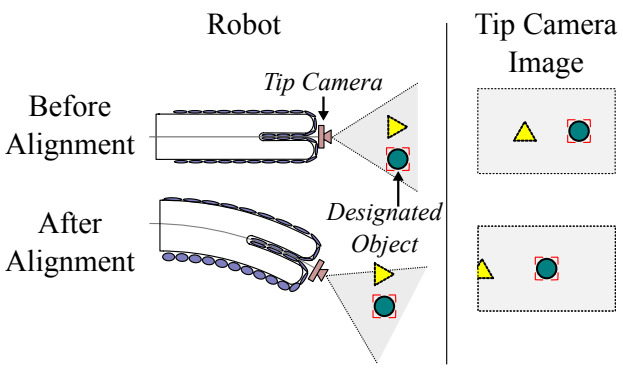

Fig. 9. Eye-in-hand visual servo control is a class of controllers that attempt to drive a designated image feature to a specified location in the camera's field of view (in our case the center). For the growing robot with a camera at its tip, this corresponds to aligning its heading with the designated feature, depicted in this figure as a circle.

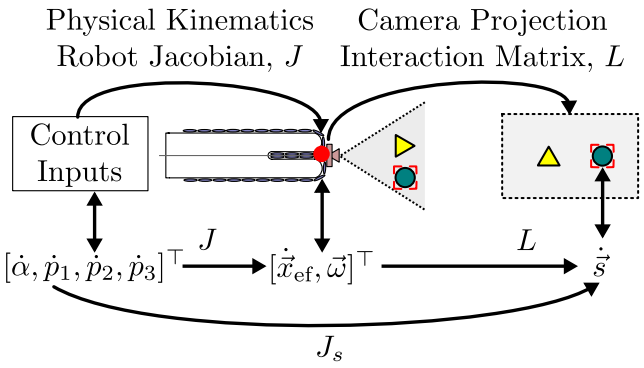

Fig. 10. Visual servo modeling components. Kinematic modeling from robot control inputs to image space consists of physical robot kinematics (Sec. III-C) and camera projection (Sec. IV-A).

coordinates of the designated object we are tracking), and we let $\vec{s}* \in \mathbb{R}^2$, be the desired coordinates of $\vec{s}$ (in this case, the center of the image, $[0,0]^\top$). We are interested in computing an image feature Jacobian, $J_s \in \mathbb{R}^{2\times 4}$, that maps joint space velocities, $\dot{\vec{q}} = [\dot{\alpha}, \dot{p}_1, \dot{p}_2, \dot{p}_3]^\top$, to image feature velocities, $\dot{\vec{s}}$:

$$\dot{\vec{s}} = J_s \dot{\vec{q}} \tag{33}$$

J_s is logically formed as the product of four matrices (Fig. 10):

$$J_s = L {}^c V_f {}^f V_n J \tag{34}$$

each described below, from right to left.

1) Physical robot Jacobian, J: $J \in \mathbb{R}^{6\times 4}$ is the physical robot Jacobian, and maps from joint space velocities to the end-effector twist (linear and angular velocities). Its computation was described in Sec. III-D.

2) End-effector twist transformation, ${}^f V_n$: ${}^f V_n \in \mathbb{R}^{6\times 6}$ is a transformation to map the end-effector twist $\in \mathbb{R}^6$ which is expressed in the global reference frame in which the kinematics are defined (Fig. 7) to the reference frame of the tip of the growing robot. In our case it is given by:

$$ {}^f V_n = \begin{bmatrix} R_{\text{ef}}^\top & \mathbf{0}^{3\times 3} \\ \mathbf{0}^{3\times 3} & R_{\text{ef}}^\top \end{bmatrix} \tag{35}$$

where R_{ef} is the orientation of the end-effector Eq. 17.

3) Camera twist transformation, ${}^c V_f$: ${}^c V_f \in \mathbb{R}^{6\times 6}$ is a twist transformation mapping from the robot tip to the camera frame. Because the camera is free to rotate about the robot's backbone axis (Fig. 11), the two frames are related by a rotation of an unknown angle, β, that must be estimated (Sec. IV-D.2):

$$ {}^c V_f = \begin{bmatrix} R_z(\beta)^\top & \mathbf{0}^{3\times 3} \\ \mathbf{0}^{3\times 3} & R_z(\beta)^\top \end{bmatrix} \tag{36}$$

4) Interaction matrix, L: L is the interaction matrix, which captures considerations of the camera formation process. In particular, it maps camera twist (expressed in the reference frame of the camera) to image feature velocities $\dot{\vec{s}}$ [29]:

$$\dot{\vec{s}} = L \begin{bmatrix} \dot{\vec{x}}_{\text{ef}} \\ \dot{\vec{\omega}} \end{bmatrix} \tag{37}$$

In our case, the image feature we wish to control is the image coordinate of the designated object that the robot is being steered toward, $\vec{s} = [s_x, s_y]^\top$. Espiau et al. have derived the interaction matrix for this case in [30] and it is given by

$$L = f \begin{bmatrix} -1/Z & 0 & x/Z & xy & -(1+x^2) & y \\ 0 & -1/Z & y/Z & 1+y^2 & -xy & -x \end{bmatrix} \tag{38}$$

where Z is the depth of the object relative to the camera and x, y are the normalized image coordinates of the goal object. They are related to pixel coordinates, $[u, v]^\top$, by the following relationship:

$$x = u/f \quad \text{and} \quad y = v/f$$

assuming the principal point of the camera is at the origin of the image, and f is the focal length of the camera in pixels.

In this work, we are interested only in the last three columns of the image space Jacobian because we would like to control the heading of the robot by modulating the pressure in each of the three sPAM actuators (p_1, p_2, p_3)

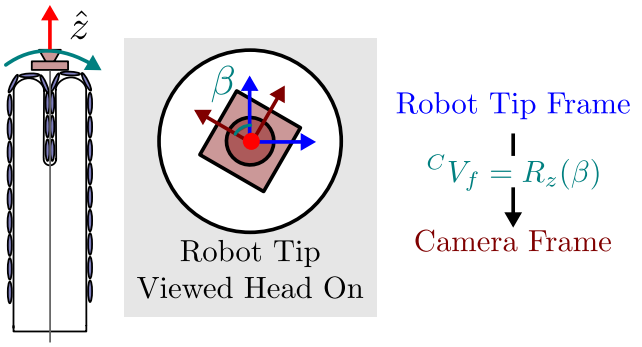

Fig. 11. Camera spin diagram. Camera is free to spin about the robot's backbone axis, $\hat{z}$, resulting in a rotation by an unknown amount β that must be estimated to compute the image Jacobian.

and not through growth (α). We will refer to the reduced column Jacobian when referencing J_s throughout the rest of the paper.

B. Growing Considerations

Consider the case that the growing robot is steering to a goal object far away ($1/Z \approx 0$). In this section, we show that the image Jacobian, J_s, scales with length. This is an important consideration for controller stability as changes in joint-space parameters have magnified effects at longer lengths. The scaling of J_s with length is explained as follows.

In the case that $1/Z \approx 0$, L reduces to

$$L \approx f \begin{bmatrix} 0 & 0 & 0 & xy & -(1+x^2) & y \\ 0 & 0 & 0 & 1+y^2 & -xy & -x \end{bmatrix} \tag{39}$$

This says that tip orientation and not tip position affect image feature coordinates (i.e. there is no parallax).

Let θ, ϕ, l be the arc-space parameters of a robot with equilibrium length l_{eq} and let θ_α, ϕ_α, l_α be the arc-space parameters of a robot with equilibrium length αl_{eq}. Then by Sec. III-C we have

$$\theta_\alpha = \alpha\theta, \quad \phi_\alpha = \phi, \quad l_\alpha = \alpha l \tag{40}$$

and therefore their velocities scale accordingly:

$$\dot{\theta}_\alpha = \alpha\dot{\theta}, \quad \dot{\phi}_\alpha = \dot{\phi}, \quad \dot{l}_\alpha = \alpha\dot{l} \tag{41}$$

It can be seen by inspection of equation 17, that the magnitude of the angular velocity vector will scale linearly with α since $\dot{\theta}$ scales linearly with α. Because L is non-zero only in the columns corresponding to angular velocity, J_s will scale linearly with α as well.

C. Visual Servo Control Law

A standard visual servo control law as presented in [30], [31] can be used to drive the image feature error magnitude $\vec{s}^* - \vec{s}$ to 0 (point the robot at the goal object):

$$\dot{\vec{q}} = \lambda J_s^+ (\vec{s}^* - \vec{s}) \tag{42}$$

where J_s^+ is the pseudo-inverse of J_s. This control law commands joint velocities that will lower the magnitude of the image feature error.

In this work, we modify the standard visual servo control law in two ways. First, we add damping to the image feature error which was empirically found to reduce controller based oscillations and limit cycles:

$$\vec{e} = K_p(\vec{s}^* - \vec{s}) + K_d\dot{\vec{s}} \tag{43}$$

where K_p is the proportional term and K_d is the damping term.

Second, we use box-constrained least squares optimization [32] to find joint velocities that will decrease the magnitude of the image error, $\vec{e}$, rather than the pseudoinverse of the image-space Jacobian. We do this because the pseudoinverse of the image Jacobian does not respect joint space limits (e.g. negative sPAM pressures are not physically realizable):

$$\dot{\vec{q}} = \underset{0 \le \vec{q} \le p_{\max}}{\arg\min} \|J_s\dot{\vec{q}} - \vec{e}\|_2 \tag{44}$$

This was empirically found to reduce the rise time/settling time of the controller and improve stability compared to the standard psuedoinverse controller with clipping to actuator limit ranges.

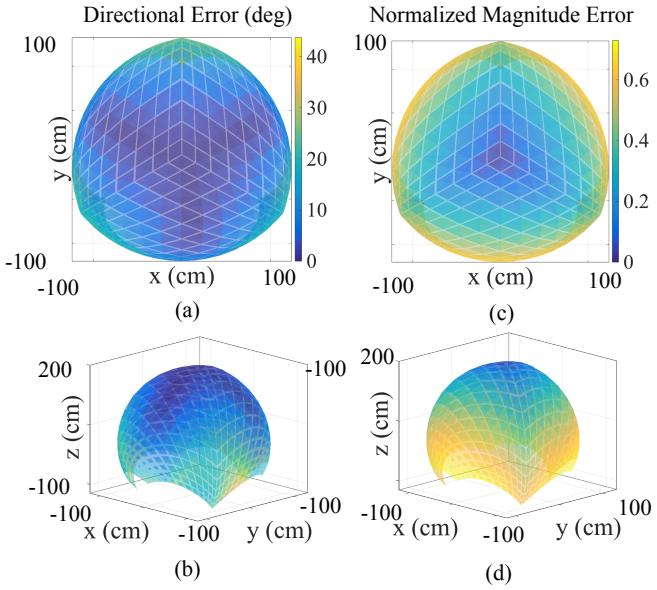

Fig. 12. Visualization of the consistency of the image Jacobian throughout the growing robot's workspace. (a) and (b) show the directional consistency from the side and above, respectively. (c) and (d) show the magnitude consistency from the side and above, respectively. Because the image Jacobian is slow to change throughout the robot's workspace, using a static Jacobian estimate in the visual servo control law (Sec. IV-C) results in a stable controller.

D. Jacobian Calibration

Our visual servo control law (Sec. IV-C) relies on an accurate image space Jacobian, J_s. Due to the number of physical parameters used to calculate J_s that may vary between uses of the robot, we have elected to use an empirical image space Jacobian, $\widehat{J}_s$, that is determined through a simple calibration process. This process is inspired by the work of Yip and Camarillo [9].

We perform the calibration process at the beginning of each use, when the robot is in a straight forward configuration. Column i of the image space Jacobian is determined by incrementing the corresponding joint space variable, q_i, by some amount δq_i and monitoring its effect on the image feature vector, $\vec{s}$:

$$\widehat{J}_s = \begin{bmatrix} \vec{J}_s^{(1)} & \vec{J}_s^{(2)} & \vec{J}_s^{(3)} \end{bmatrix} \tag{45}$$

$$\vec{J}_s^{(i)} = \frac{\delta\vec{s}}{\delta q_i} \tag{46}$$

$$\delta\vec{s} = \vec{s} - \vec{s}_0 \tag{47}$$

where $\vec{s}_0$ are the image coordinates of the designated object in its beginning location.

1) Configuration Considerations: $\widehat{J}_s$ is used in place of J_s in the visual servo control law (Sec. IV-C). We note that J_s is a function of its state, and therefore varies throughout its workspace, yet $\widehat{J}_s$ is calibrated to J_s only in the straight-forward configuration before growth. However, we have found that this Jacobian results in stable control. This is due to the consistency of the image Jacobian throughout the robot's workspace. Fig. 12 shows an analysis of how well the image Jacobian in the straight-forward configuration approximates the image Jacobian throughout its workspace. Both magnitude errors and direction errors were considered. Normalized magnitude errors at each configuration were calculated as:

$$\text{mean}\left(|\vec{J}_s^{(i)}|_2 - |\vec{J}_{s0}^{(i)}|_2\right) / \text{mean}\left(|\vec{J}_s^{(i)}|_2\right) \quad \text{for i=1,2,3} \tag{48}$$

and direction errors were calculated as:

$$\text{mean}\left(\angle(\vec{J}_s^{(i)}, \vec{J}_{s0}^{(i)})\right) \quad \text{for i=1,2,3} \tag{49}$$

where J_s is the image Jacobian at a particular configuration, J_{s0} is the image Jacobian in the straight forward configuration, and $\vec{J}_s^{(i)}, \vec{J}_{s0}^{(i)}$ are the ith column of J_s and J_{s0}, respectively.

Using this analysis, we find that if J_{s0} is used to approximate the Jacobian throughout the workspace, the magnitude of the Jacobian will differ by as much as a factor of 0.7 and the direction by as much as $40°$. Unsurprisingly, J_{s0} becomes a less accurate approximation at the edges of the workspace (further away from the straight-forward configuration).

Performing the same analysis for the physical robot Jacobian, we find that it varies much more throughout the robot's workspace than the image space Jacobian. In particular, the physical robot Jacobian in the straight-forward configuration differs by as much as a factor of 2 in magnitude and $110°$ in direction when used to approximate the physical robot Jacobian throughout its workspace. This discrepancy is large enough that an equivalent calibration routine would not work for task-space control of this robot. Instead a configuration dependent, model-based Jacobian relying on known physical parameters that may change between uses of the robot would have to be used.

Another configuration consideration is robot length. $\hat{J}_s$ is calibrated before growth and the length of the robot will continually increase during the growth process, which affects the image space Jacobian. As explained in Sec. IV-B, the magnitude of J_s approximately scales with length. To account for this and inaccuracies in the calibrated Jacobian, $\widehat{J}_s$, we choose controller gains K_p, K_d (Sec. IV-C) that are more conservative than the optimal gains for steering of the robot just after Jacobian calibration. Concretely, if K_p^* and K_d* are the optimal gains for steering just after calibration, we set $K_p, K_d = K_p^*/2, K_d^*/2$.

2) Camera Rotation: As explained in Sec. IV-A.3, the camera is free to rotate about its optical axis as the robot grows (Fig. 11). Rotations about the optical axis are captured by the parameter β, which is the angle between the robot tip frame and camera reference frame. β is initially $0°$. To account for camera rotation, $\widehat{J}_s$ must be continually updated to compensate for changes in β.

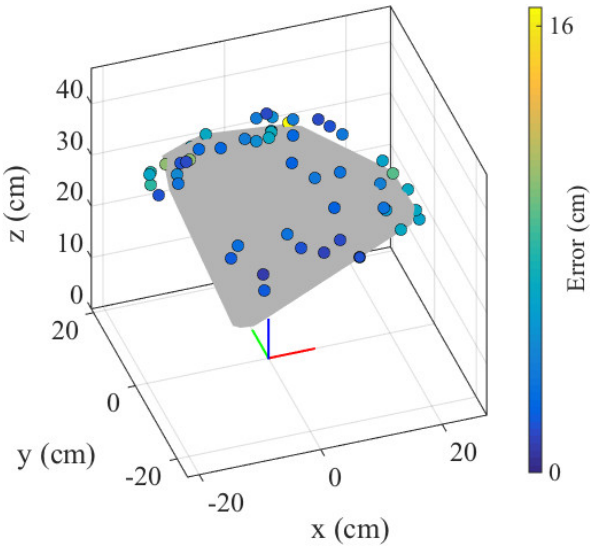

Fig. 13. Results of the verification experiment for the model of steering kinematics. Measured end-effector positions for 50 random pressure triples are displayed as solid circles. Parameter identification was performed to determine parameters that best fit the measured positions. The resulting workspace is shown in grey and was calculated using the kinematic model. The color of each solid circle represents the distance between the position predicted by the kinematic model and the measured position.

To estimate β, we use an inertial measurement unit (IMU, Bosch BNO055) rigidly attached to the tip camera. The IMU provides an estimate of the direction of gravity, $\hat{g} = [g_x, g_y, g_z]^\top$, in the reference frame of the camera. β is computed from $\hat{g}$ by computing the angle of its two-dimensional projection onto the plane of the camera:

$$\beta = \text{atan2}(g_y, g_x) - \text{atan2}(g_y^0, g_x^0) \tag{50}$$

where $\hat{g}^0 = [g_x^0, g_y^0, g_z^0]^\top$ is the gravity vector when the tip frame and camera reference frame are aligned, i.e. $\beta = 0$. With an estimate of β, $\widehat{J}_s$ is compensated to account for camera spin by a two-dimensional rotation:

$$\widehat{J_s^c} = \begin{bmatrix} \cos(\beta) & \sin(\beta) \\ -\sin(\beta) & \cos(\beta) \end{bmatrix} \widehat{J}_s \tag{51}$$

where $\widehat{J_s^c}$ is the compensated image Jacobian. This update equation is equivalent to updating ${}^C V_f$ with the new value of β in Eq. 34.

V. Experimental Results

In this section we present experiments that both characterize the growing robot and validate the kinematic models and control presented in this work.

A. Kinematic Model Validation

To verify the model of steering kinematics presented in Sec. III-B, an electromagnetic tracker (Ascension Model 800, Northern Digital Incorporated, Waterloo, ON, Canada) was attached near the tip of a growing robot that was held at

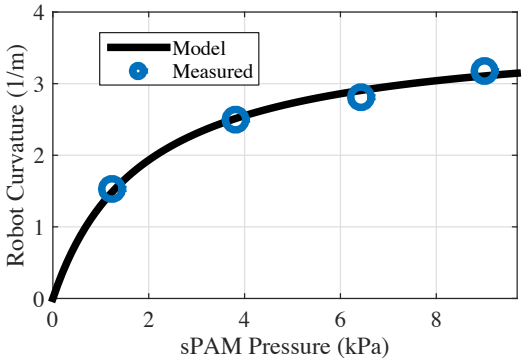

Fig. 14. Shows the effect of a single sPAM actuator on robot bending. The curvature predicted by the kinematic model is shown in black and the measured curvature is shown in blue. Curvature increases with sPAM pressure, but saturates as the sPAM reaches its maximum contraction ratio.

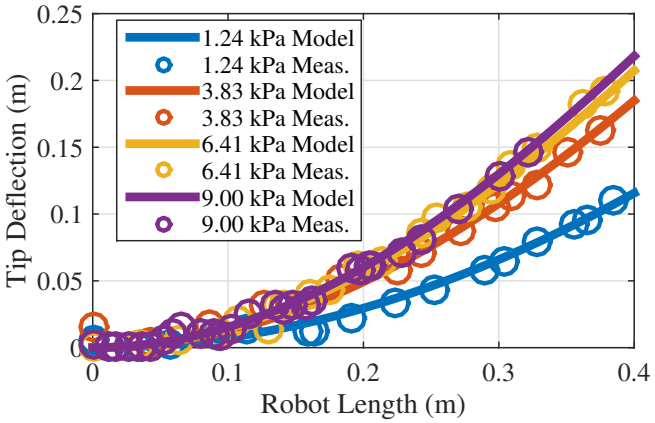

Fig. 15. Tip deflection from a straight line trajectory versus length. Robot was grown four times with four different sPAM pressure values. Expected tip deflection for a robot grown with four sPAM pressures are plotted in solid lines and corresponding measurements are shown as circles of the same color. Model and measurements indicate robot grows with constant curvature with curvature predicted by plot in Fig. 14.

a constant length of approximately 42 cm. We commanded 50 random sPAM pressure triples (p_1, p_2, p_3) and recorded the pose of the robot end effector once it reached steady state.

Actuator positions, ψ_i, were measured by commanding a displacement in each of the primary directions ($[p_1 = P, p_2 = 0, p_3 = 0]^\top$, $[p_1 = 0, p_2 = P, p_3 = 0]^\top$ and $[p_1 = 0, p_2 = 0, p_3 = P]^\top$). A parameter identification was then performed to find actuator and main tube equilibrium lengths, pressure spring constant factor (Equation 3), and main tube linear and torsion spring constants. The parameter identification was solved by finding the aforementioned parameter values that minimized the discrepancy between the predicted end-effector positions and measured end-effector positions. This was implemented using MATLAB's `fmincon` routine.

With the parameter identification complete, we compared the predicted and measured robot end-effector position for each pressure triple. The 50 circles in Fig. 13 show the measured positions of the robot's end-effector, and the color represents the distance between the position predicted by the kinematic model and the measured position. We found a mean discrepancy of 5.5 cm between prediction and measurement, which is slightly larger than the pneumatic backbone's diameter (4.8 cm). Fig. 13 shows the robot's approximate workspace in dark-grey. It was calculated by determining the end-effector position for randomly sampled pressure triples using the kinematic model and identified parameters.

B. Growing Kinematics Validation

We performed an experiment to verify the analysis of growth for the kinematic model presented in Sec. III-C. In this experiment, the robot was grown four separate times with constant sPAM pressures of 0.18, 0.555, 093, and 1.305 pounds per square inch (PSI) respectively in a single sPAM. These pressures were chosen to provide significant coverage of the curvature range. An overhead camera recorded the movement of the robot during the growth. Manual segmentation of the tip of the robot was performed roughly every 4 cm to yield a time-series of tip positions of the robot as it was grown. At the end of each trial, a curvature value was fit to the backbone of the grown robot using manual segmentation and the results are shown as blue circles in Fig. 14.

Rearrangement of the kinematic model equations (Eqs. 7,13,14) results in an equation that predicts the growing robot backbone curvature as a function of sPAM pressure:

$$\kappa = \frac{k_1 p}{k_2 p + 1} \tag{52}$$

where k_1, k_2 are constants that depend on the physical parameters of the robot, p is the pressure in the sPAM and κ is the backbone curvature of the growing robot. k_1, k_2 were chosen to minimize the difference between the predicted curvature values and four measured curvature values. The resulting curve is shown in Fig. 14. The robot starts straight (zero curvature) when there is no pressure in the sPAMs. Curvature increases rapidly at low pressure values, but saturates due to the finite strain that is achievable by an sPAM.

Based on the fit curvature values, we predicted the expected tip deflection from a straight-line trajectory over the course of the four growth trials. According to Sec. III-C, we expect the robot to grow with constant curvature since the pressure in the sPAMs was held constant. Fig. 15 shows the predicted tip deflection values along with measured tip deflection values as a function of backbone length. As can be seen, there is strong agreement between predicted and measured tip deflection, indicating that the robot does grow with constant curvature, as predicted.

C. sPAM Dynamic Response

We performed an experiment to measure the dynamic response of open-loop bending of the growing robot held at a constant length. To understand how length affected the bending behavior of the robot, we generated experimental

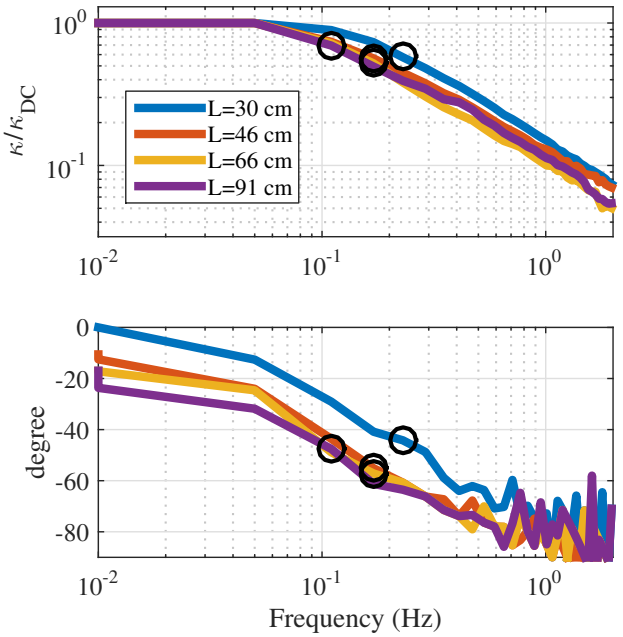

Fig. 16. Bode plot of open loop robot bending (frequency versus backbone curvature amplitude) for several robot lengths. The robot exhibits first order system behavior with a phase loss of approximately 90 degrees and cutoff frequency at approximately 45 degree phase loss for all four tested robot lengths. Unsurprisingly, cutoff frequency drops with length indicating that the robot is capable of less responsive steering at larger lengths.

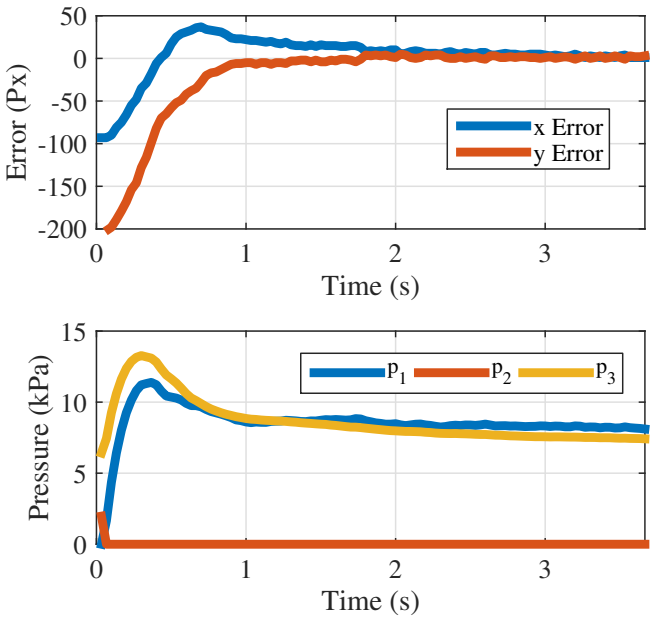

Fig. 17. Visual servo control step response. At time $t = 0$ a new visual feature is designated. By time $t = 2$, the step response pixel error (a) is less than 5% indicating that the robot is pointing at the visual feature. Commanded sPAM pressures are shown in (b).

Bode plots of bending curvature versus frequency of growing robots of four different lengths: 30, 46, 66, and 91 inches. A red and blue colored fiducial were attached to the tip of the robot several centimeters apart along its backbone to facilitate automated measurement of tip orientation using an overhead camera. A sinusodial sweep of pressures in a frequency range of 0 to 2 Hz was commanded to create a sinusoidally varying backbone curvature. Two sPAMs placed radially opposite one another were used in the experiment so that bending in opposite directions could occur ($\phi = 0°, 180°$).

Curvature amplitude was measured from tip orientation at a particular frequency, ω, by setting $\kappa_\omega = (\theta_{\max} - \theta_{\min})/2$ where $\theta_{\max}, \theta_{\min}$ were the maximum and minimum tip orientations measured in the ω frequency portion of the sinusoidal sweep. Phase information was extracted using a light emitting diode that was activated at the beginning of a new frequency so that precise synchronization between the video and commanded pressures could be determined. Fig. 16 shows the experimental Bode plot of normalized curvature vs frequency for each of the four lengths.

All four robot lengths had a cutoff frequency (frequency at which curvature magnitude ratio drops below $1/\sqrt{2}$) of less than 0.5 Hz (indicated by the black circles in Fig. 16), with cutoff frequency monotonically decreasing with increasing robot length. Dynamic response is most likely limited by flow rate of the regulators used to inflate the sPAMs. Though the robot has low bandwidth in the large curvature changes that are needed for volitional direction changes of the robot, its bandwidth is higher for smaller amplitude curvature changes, which are needed to maintain heading alignment during robot growth.

D. Visual Servo Control Validation

Fig. 17 shows data taken from a point-to-point tracking without growth ($\dot{\alpha} = 0$). At time $t = 0$, a new feature is designated, providing a step input to the controller. As shown in Fig. 17(a), the controller drives the image feature error to below 5% within 2 seconds, resulting in a rise and settling time of under 2 seconds. Rise time and settling time are limited by the maximum flow rate of the proportional valves used in this work (Sec. II-B).

E. Growing to a Goal Location

Several experiments were performed to demonstrate the robot's ability to grow and steer to a designated object using the visual servo control law described in Sec. IV-C.

Fig. 19 shows a sequence of still-frame images of the robot growing to a light as well as the pressures that were commanded by the visual servo steering controller. The corresponding pressure plot shows the robot starting with high pressure in two of its three sPAMs. These sPAM pressures cause the robot to bend so that its heading is aligned with the light. As the robot lengthens, the steering controller decreases pressure in its sPAMs to maintain a straight-line trajectory that is aligned with the light. If it did not lower pressure, the robot would oversteer, as seen in Fig. 15. The visual servo controller is able to accomplish this behavior by maintaining the light at the center of its tip camera image without explicit consideration of growth or curvature.

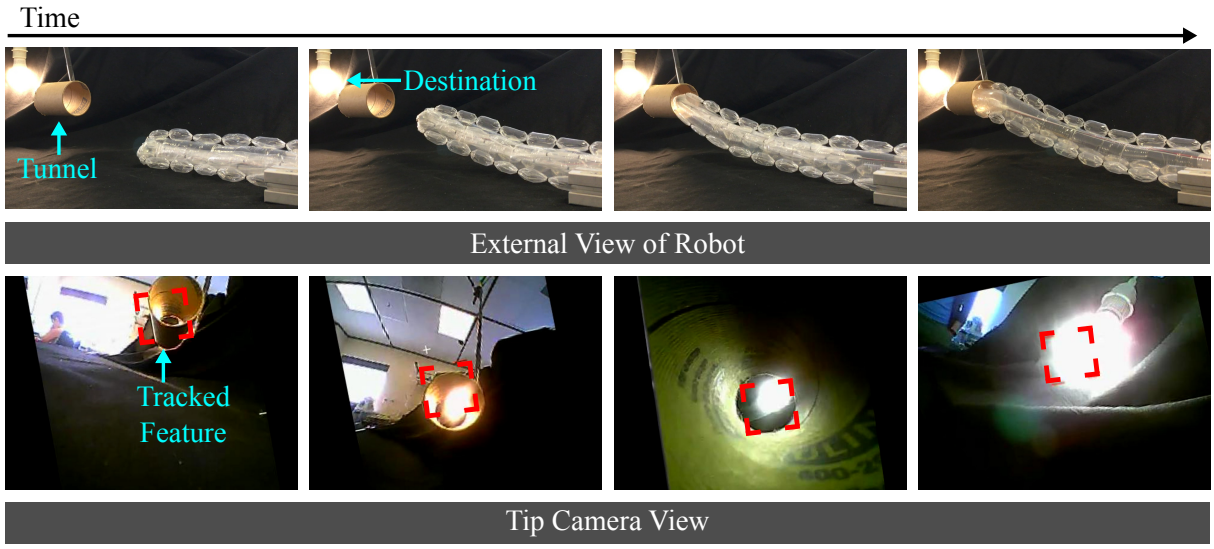

Fig. 18. Two image sequences showing the robot growing to a light via a tunnel. Top row is an image sequence of the robot and bottom row is an image sequence from the robot's tip camera. Each image pair in a column is time-aligned. Time progresses to the right, and the first image is from the moment after the steering controller was turned on. The right-most image is an overhead view of the robot.

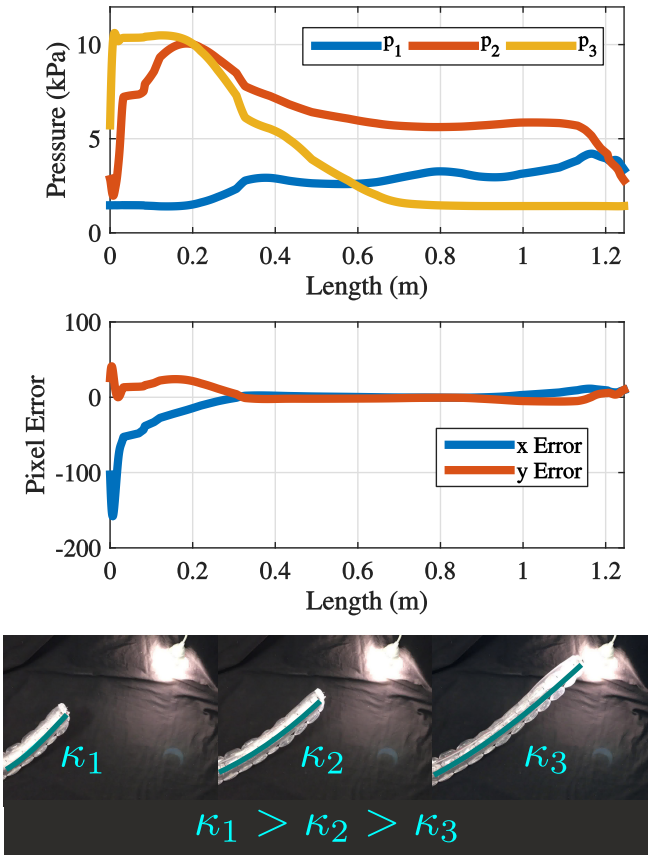

Fig. 19. Growing and steering to a light. To maintain heading alignment with the light as the robot's length increases, the steering controller must continually decrease the curvature of the robot by decreasing the pressure in the sPAMs. This behavior is not explicitly programmed in the visual servo control law, but happens as an indirect consequence of keeping the light at the center of its tip camera image (indicated by zero pixel error). Still-frame images are shown at three times during its growth with corresponding decreasing curvatures $\kappa_1, \kappa_2, \kappa_3$.

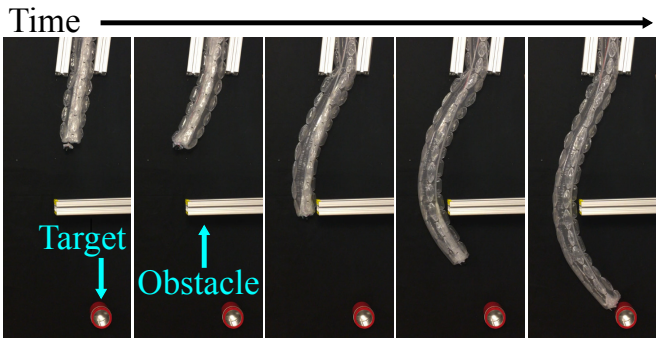

Fig. 20. Growth around an obstacle. First the robot is steered to a waypoint to the left of the obstacle and then to the destination.

More complicated growth trajectories are shown in Figs. 18 and 20. Both figures feature the robot's ability to navigate paths which are not constant curvature. In Fig. 18, the robot is first steered into a tunnel by designating the tunnel's entrance as the tracked feature for the visual servo controller. Once inside the tunnel, the controller's destination was changed to the light. Though the robot's body is constrained by the tunnel, it is able to grow to a new destination after laving the tunnel without modification to the control law. In Fig. 20, the robot must first make it around an obstacle before reaching its destination. To accomplish this, the robot was first steered to a waypoint to the left of the obstacle before being steered to its destination. In both cases, the visual servo controller is successful even though the robot takes on non-constant curvature shapes.

VI. Conclusions and Future Work

This paper presents the design, modeling, and control of a new soft continuum robot that has a novel extension degree of freedom. The extension degree of freedom provides a

direction of movement that is always tangent to the robot's backbone. Among other benefits, it simplifies the control of the robot by decoupling steering and movement. Extension of the robot is realized using pneumatically driven tip eversion.

Though extension was limited to 100% of original body length in this paper, Hawkes et al. demonstrated that pneumatically driven tip eversion can be used to grow a robot's length by several orders of magnitude [10]. In addition, it was found that tip eversion is advantageous for moving through cluttered and inhomogeneous environments since it can penetrate tight spaces and the robot's body does not use external reaction forces to move.

Instead of turning the robot at discrete intervals along its length, which irreversibly changes its shape, the robot introduced in this paper steers using reversible bending of the robot's backbone to deflect the robot from a straight path. There are several tradeoffs between the two methods of steering that may make one mechanism more advantageous for a given use-case. Reversible turning gives the operator the ability to look around the robot's environment by reorienting the robot's tip. In addition, corrections to the robot's heading can be made as the robot is growing, which is particularly advantageous for scenarios where accurate alignment is needed, such as growing into a tunnel (Fig. 18).

On the other hand, because the entire length of the robot may move when the backbone is bent, environmental contacts affect the robot's steering behavior more than the robot in [10]. Additionally the robot in [10] is nonholonomic, which has the advantage that the robot body does not move once it is grown, but has the disadvantage that the robot must grow to turn. Because steering decisions are made at discrete intervals and are permanent, stability of the steering controller is not a concern for the irreversible turning mechanism. This is not the case for the robot in this work, where steering gains must be selected with care (Sec. IV-C). Ultimately the optimal turning solution for growing robots may be a combination of the turning mechanisms presented in this paper and [10]. Future work will investigate new actuator design and control that combines features of both steering methods.

REFERENCES

[1] J. Burgner-Kahrs, D. C. Rucker, and H. Choset, "Continuum robots for medical applications: A survey," *IEEE Transactions on Robotics*, vol. 31, no. 6, pp. 1261–1280, 2015.

[2] P. E. Dupont, J. Lock, B. Itkowitz, and E. Butler, "Design and control of concentric-tube robots," *IEEE Transactions on Robotics*, vol. 26, no. 2, pp. 209–225, 2010.

[3] R. J. Webster III, J. M. Romano, and N. J. Cowan, "Mechanics of precurved-tube continuum robots," *IEEE Transactions on Robotics*, vol. 25, no. 1, pp. 67–78, 2009.

[4] S. Neppalli, B. Jones, W. McMahan, V. Chitrakaran, I. Walker, M. Pritts, M. Csencsits, C. Rahn, and M. Grissom, "Octarm-a soft robotic manipulator," in *IEEE/RSJ International Conference on Intelligent Robots and Systems*, 2007, pp. 2569–2569.

[5] J. S. Mehling, M. A. Diftler, M. Chu, and M. Valvo, "A minimally invasive tendril robot for in-space inspection," in *IEEE/RAS-EMBS International Conference on Biomedical Robotics and Biomechatronics*, 2006, pp. 690–695.

[6] I. D. Walker, "Continuous backbone continuum robot manipulators," *ISRN Robotics*, 2013.

[7] R. J. Webster and B. A. Jones, "Design and Kinematic Modeling of Constant Curvature Continuum Robots: A Review," *The International Journal of Robotics Research*, vol. 29, no. 13, pp. 1661–1683, 2010.

[8] I. A. Gravagne, C. D. Rahn, and I. D. Walker, "Large deflection dynamics and control for planar continuum robots," *IEEE/ASME transactions on mechatronics*, vol. 8, no. 2, pp. 299–307, 2003.

[9] M. C. Yip and D. B. Camarillo, "Model-less feedback control of continuum manipulators in constrained environments," *IEEE Transactions on Robotics*, vol. 30, no. 4, pp. 880–889, 2014.

[10] E. W. Hawkes, L. H. Blumenschein, J. D. Greer, and A. M. Okamura, "A soft robot that navigates its environment through growth," *Science Robotics*, vol. 2, no. 8, p. eaan3028, 2017.

[11] D. Mishima, T. Aoki, and S. Hirose, "Development of pneumatically controlled expandable arm for search in the environment with tight access," in *Field and Service Robotics*. Springer, 2003, pp. 509–518.

[12] T. Rösch, A. Adler, H. Pohl, E. Wettschureck, M. Koch, B. Wiedenmann, and N. Hoepffner, "A motor-driven single-use colonoscope controlled with a hand-held device: a feasibility study in volunteers," *Gastrointestinal endoscopy*, vol. 67, no. 7, pp. 1139–1146, 2008.

[13] A. Sadeghi, A. Tonazzini, L. Popova, and B. Mazzolai, "Robotic mechanism for soil penetration inspired by plant root," in *Robotics and Automation (ICRA), 2013 IEEE International Conference on*. IEEE, 2013, pp. 3457–3462.

[14] ——, "A novel growing device inspired by plant root soil penetration behaviors," *PloS one*, vol. 9, no. 2, 2014.

[15] E. Del Dottore, A. Mondini, A. Sadeghi, V. Mattoli, and B. Mazzolai, "Circumnutations as a penetration strategy in a plant-root-inspired robot," in *IEEE International Conference on Robotics and Automation (ICRA)*, 2016, pp. 4722–4728.

[16] H. Tsukagoshi, N. Arai, I. Kiryu, and A. Kitagawa, "Tip growing actuator with the hose-like structure aiming for inspection on narrow terrain." *International Journal of Automation Technology*, vol. 5, no. 4, pp. 516–522, 2011.

[17] J. D. Greer, T. K. Morimoto, A. M. Okamura, and E. W. Hawkes, "Series pneumatic artificial muscles (sPAMs) and application to a soft continuum robot," in *IEEE International Conference on Robotics and Automation (ICRA)*, 2017, pp. 5503–5510.

[18] D. B. Camarillo, C. F. Milne, C. R. Carlson, M. R. Zinn, and J. K. Salisbury, "Mechanics modeling of tendon-driven continuum manipulators," *IEEE Transactions on Robotics*, vol. 24, no. 6, pp. 1262–1273, 2008.

[19] C.-P. Chou and B. Hannaford, "Measurement and modeling of mckibben pneumatic artificial muscles," *IEEE Transactions on Robotics and Automation*, vol. 12, no. 1, pp. 90–102, 1996.

[20] G. K. Klute, J. M. Czerniecki, and B. Hannaford, "Mckibben artificial muscles: pneumatic actuators with biomechanical intelligence," in *IEEE/ASME International Conference on Advanced Intelligent Mechatronics*, 1999, pp. 221–226.

[21] R. Niiyama, X. Sun, C. Sung, B. An, D. Rus, and S. Kim, "Pouch motors: Printable soft actuators integrated with computational design," *Soft Robotics*, vol. 2, no. 2, pp. 59–70, 2015.

[22] F. Daerden, "Conception and realization of pleated pneumatic artificial muscles and their use as compliant actuation elements," *Vrije Universiteit Brussel, Belgium*, 1999.

[23] E. W. Hawkes, D. L. Christensen, and A. M. Okamura, "Design and implementation of a 300% strain soft artificial muscle," in *IEEE International Conference on Robotics and Automation*. IEEE, 2016, pp. 4022–4029.

[24] N. S. Usevitch, A. M. Okamura, and E. W. Hawkes, "Antagonistic pneumatic artificial muscle," in *IEEE International Conference on Robotics and Automation*, 2018.

[25] G. Flandin, F. Chaumette, and E. Marchand, "Eye-in-hand/eye-to-hand cooperation for visual servoing," in *IEEE International Conference on Robotics and Automation*, vol. 3, 2000, pp. 2741–2746.

[26] F. Daerden and D. Lefeber, "The concept and design of pleated pneumatic artificial muscles," *International Journal of Fluid Power*, vol. 2, no. 3, pp. 41–50, 2001.

[27] B. A. Jones, W. McMahan, and I. D. Walker, "Practical kinematics for real-time implementation of continuum robots," *Proceedings - IEEE International Conference on Robotics and Automation*, no. 6, pp. 1840–1847, 2006.

[28] L. L. Howell, *Compliant Mechanisms*. John Wiley & Sons, 2001.

[29] K. Ikeuchi, *Computer vision: A reference guide*. Springer Publishing Company, Inc., 2014.

[30] B. Espiau, F. Chaumette, and P. Rives, "A new approach to visual servoing in robotics," *ieee Transactions on Robotics and Automation*, vol. 8, no. 3, pp. 313–326, 1992.

[31] F. Chaumette and S. Hutchinson, "Visual servo control. i. basic approaches," *IEEE Robotics & Automation Magazine*, vol. 13, no. 4, pp. 82–90, 2006.

[32] P. B. Stark and R. L. Parker, "Bounded-variable least-squares: an algorithm and applications," *Computational Statistics*, vol. 10, pp. 129–129, 1995.